J. Fluid Mech. (1986), *vol.* 168, *pp.* 393–413
Printed in Great Britain

On the vorticity dynamics of a turbulent jet in a crossflow

By R. I. SYKES, W. S. LEWELLEN AND S. F. PARKER

Aeronautical Research Associates of Princeton, Inc., P.O. Box 2229,
50 Washington Road, Princeton, New Jersey 08540

(Received 26 March 1985 and in revised form 7 November 1985)

We present numerical solutions of the fully three-dimensional flow of a round, turbulent jet emitted normal to a uniform free stream. Comparisons with available laboratory data and comparison between different numerical grid resolutions are used to demonstrate the quality of the simulation. Examination of the detailed flow pattern within a computational domain, which extends 15 jet diameters from the source allows us to follow the vorticity dynamics in the transition from an initially vertical jet to a wake with a vortex pair essentially aligned with the free stream. The transition is presented as a function of the ratio of the jet exit velocity to free stream velocity. For large velocity ratios, the source of the streamwise vorticity in the vortex pair can be readily traced back to the original streamwise vorticity in the sides of the vertical jet.

1. Introduction

The introduction of a jet of fluid transversely into a moving stream is a basic configuration which finds application in many engineering fields, e.g. discharge of effluent in the atmosphere or ocean and VTOL aerodynamics. Several experimental studies (e.g. Keffer & Baines 1963; Kamotani & Greber 1972; Moussa, Trischka & Eskinazi 1977; Andreopoulos & Rodi 1984) have revealed some of the essential features of the dynamics, which are fully three-dimensional and consequently difficult to visualize. The most striking feature is the transition from an initially vertical jet through a bending phase during which the jet becomes parallel with the free stream and forms a vortex pair aligned with the flow. The details of the transition are complicated and not well understood, and we hope to shed some further light on the process in this paper.

We shall present results from numerical calculations which complement the previously mentioned experimental results. We will treat the numerical model, which allows for very detailed examination of the flow field, in much the same way one would a laboratory model. The principal result from the numerical model will be a complete picture of the flow. This detailed view has not been available from the relatively low-resolution numerical results previously published (Patankar, Basu & Alpay 1977; Chien & Schetz 1975; Demuren 1983).

2. Numerical model

We take the incompressible, Navier–Stokes equations in the form

$$\frac{\partial U_i}{\partial t}+U_j\frac{\partial U_i}{\partial x_j}=-\frac{\partial P}{\partial x_i}+\frac{\partial \tau_{ij}}{\partial x_j}, \tag{2.1}$$

$$\frac{\partial U_i}{\partial x_i}=0, \tag{2.2}$$

where U_i is the velocity vector, P the dynamic pressure, and τ_{ij} represents the stress tensor. We consider high-Reynolds number flows, so that τ_{ij} is the Reynolds stress, and U_i is the average velocity.

We use a quasi-equilibrium version of the Reynolds-stress closure model described by Lewellen (1977) to obtain the stresses in (2.1); this model is very similar to the level -2.5 model of Mellor & Yamada (1974). Specifically, we use a dynamic equation to predict the turbulent kinetic energy in the form

$$\frac{\partial q^2}{\partial t}+U_j\frac{\partial q^2}{\partial x_j}=2\tau_{ij}\frac{\partial U_i}{\partial x_j}+v_c\frac{\partial}{\partial x_i}q\Lambda\frac{\partial q^2}{\partial x_i}-2\frac{bq^3}{\Lambda}, \tag{2.3}$$

where $q^2=\overline{u_i' u_i'}$, i.e. twice the turbulent energy (the prime denotes a fluctuation about the mean value, and the overbar is the averaging operator), and Λ is a turbulence lengthscale.

The Reynolds stresses are modelled as

$$\tau_{ij}=q\frac{\Lambda}{4}\left(\frac{\partial U_i}{\partial x_j}+\frac{\partial U_j}{\partial x_i}\right), \tag{2.4}$$

and the empirical constants v_c and b are set at 0.3 and 0.125 respectively. The lengthscale Λ is determined by the geometry of the problem, and in the results presented here we set

$$\Lambda=0.25\,D+0.025\,r, \tag{2.5}$$

where D is the diameter of the jet source and r is the distance from the centre of the source. The coefficients were chosen to give a good fit to the prediction for the straight jet. Equation (2.5) is a very crude estimate, since we can not expect the scale to behave as simply in a complex three-dimensional flow; however, we believe it is adequate to simulate the essential features of the bending phase of the jet evolution.

In addition to the momentum equations, we also calculate a passive scalar field from the conservation equation

$$\frac{\partial C}{\partial t}+U_j\frac{\partial C}{\partial x_j}=\frac{\partial F_j}{\partial x_j}, \tag{2.6}$$

where the scalar flux is modelled as

$$F_j=\frac{q\Lambda}{3}\frac{\partial C}{\partial x_j}. \tag{2.7}$$

The above equations are discretized onto a grid using centred spatial differencing on a non-uniform mesh and leapfrog time-differencing. The difference equations are very similar to those used by Mason & Sykes (1979); the absolutely conserving scheme of Piacsek & Williams (1970) is used to represent the advection terms, and the diffusive terms are approximated with the DuFort–Frankel scheme. The Poisson equation for the pressure is solved using the direct technique due to Farnell (1980).

An additional numerical technique was employed to obtain the steady-state solution as quickly as possible. The effective timestep was made a function of space, so that it could increase downstream from the jet as the streamwise gridlength (and hence, the associated Courant limit) increased. It proved possible to use the direct Poisson solver, provided that the timestep was a separable function of the three spatial coordinates. In the runs reported here, the strictest timestep criterion was set by the Courant condition in the fine mesh at the jet exit, but this was allowed to increase in proportion to the local streamwise grid length up to a factor of 6 above the minimum condition. This allowed steady calculations to be made with 500 timesteps, rather than the 1500 steps using the small timestep everywhere.

Boundary conditions on the model were as follows:

(*a*) Inflow boundary $x = X_1$

$$U = U_0, \quad V = W = C = q^2 = 0;$$

(*b*) Outflow boundary $x = X_2$

$$\frac{\partial V}{\partial x} = \frac{\partial W}{\partial x} = \frac{\partial C}{\partial x} = \frac{\partial q^2}{\partial x} = 0;$$

$$U_B^{t+1} = U_{B-1}^t,$$

where t represents the time level, and B represents the boundary point;

(*c*) Lower boundary $z = 0$

$$\left.\begin{aligned} U = V &= 0 \\ W &= W_0 \\ C &= C_0 \\ q^2 &= q_0^2 \\ W &= 0 \end{aligned}\right\} \quad |x^2+y^2| < \tfrac{1}{4}D^2,$$

$$\frac{\partial U}{\partial z} = \frac{\partial V}{\partial z} = \frac{\partial C}{\partial z} = \frac{\partial q^2}{\partial z} = 0, \quad |x^2+y^2| \geqslant \tfrac{1}{4}D^2,$$

where D is the jet exhaust diameter;

(*d*) Upper boundary $z = Z_2$

$$W = 0,$$

$$\frac{\partial U}{\partial x} = \frac{\partial V}{\partial z} = \frac{\partial C}{\partial z} = \frac{\partial q^2}{\partial z} = 0;$$

(*e*) Lateral boundaries $y = 0, Y_2$

$$V = 0,$$

$$\frac{\partial U}{\partial y} = \frac{\partial W}{\partial y} = \frac{\partial C}{\partial y} = \frac{\partial q^2}{\partial y} = 0.$$

We note that the outflow boundary condition is a very crude type of open condition (cf. Orlanski 1976); however, since virtually all such conditions give a zero-slope condition in the steady state, it is of little consequence provided that it does not disrupt the transient unduly. The simple condition adequately handles the passage of the jet.

Run	X_1	X_2	Y_2	Z_2	Nx	Ny	Nz
R2	−3	16	4	4.9	39	18	30
R4	−3	16	8	12	39	20	30
R8	−3	16	14	20	39	20	30
R8: High resolution	−3	16	14	20	66	35	50

TABLE 1.

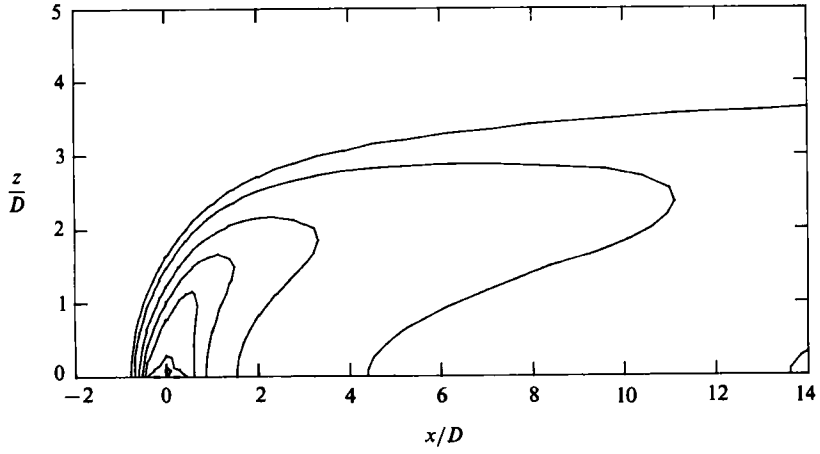

FIGURE 1. Dimensionless scalar field in the plane $y = 0$ for $R = 2$. Contour interval 0.1.

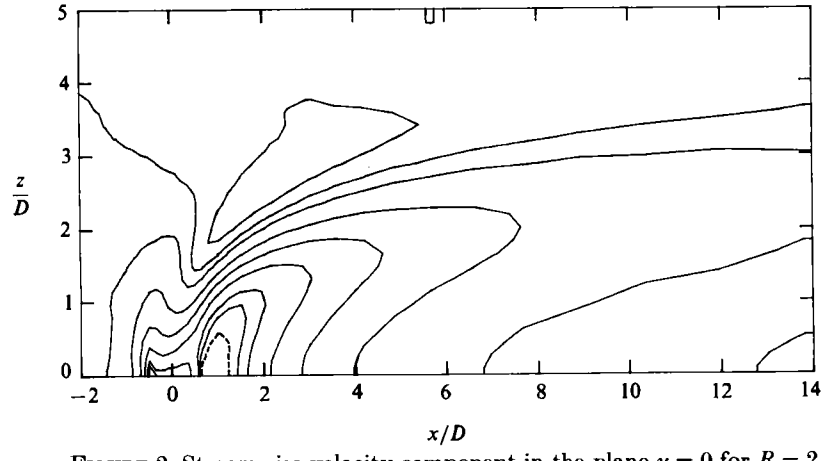

FIGURE 2. Streamwise velocity component in the plane $y = 0$ for $R = 2$. Contour interval 0.1, negative values shown dashed.

Furthermore, we do not treat the lower surface as true wall outside the jet-exhaust region; instead, it is a stress-free wall. This is because a real wall introduces a local boundary layer, which needs to be resolved by the numerical mesh, and since our main interest is in jets remote from a wall, we have not attempted to model this region accurately.

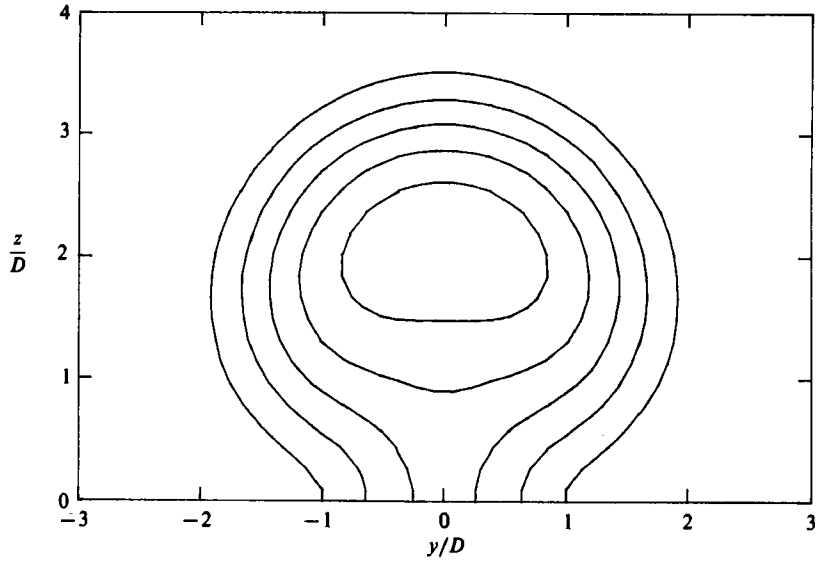

FIGURE 3. Transverse section of the scalar field at $x = 6$ for $R = 2$. Contour interval 0.05.

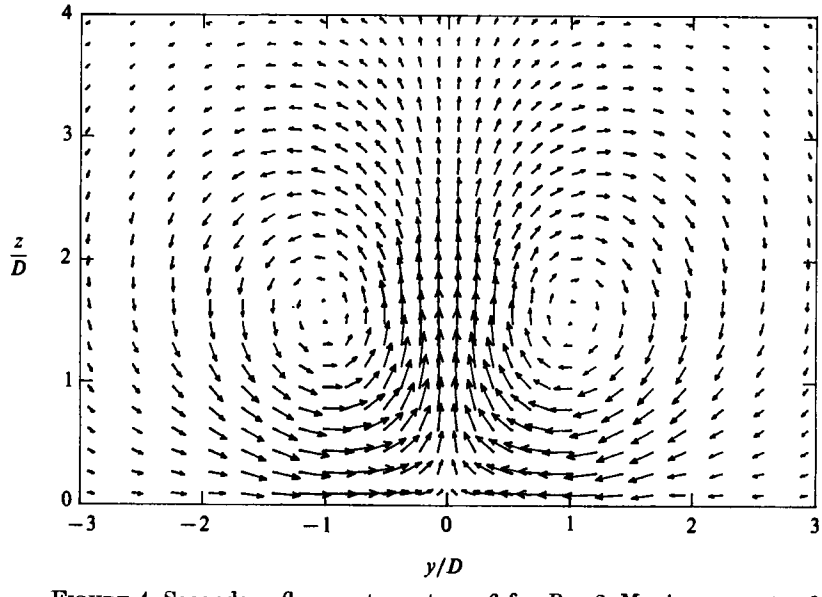

FIGURE 4. Secondary flow vectors at $x = 6$ for $R = 2$. Maximum vector 0.2.

3. Results

Our ultimate objective in the development of this numerical model will be a better understanding of plumes from tall stacks in the atmosphere; hence we only consider relatively large jet exit ratios, W_0/U_0; in fact, we present results for $W_0/U_0 = 2$, 4, and 8. This is the justification for our simple treatment of the lower boundary. Table 1 shows the numerical parameters for four calculations; note that the only physical parameters are the inflow velocity U_0 and the diameter D, which we can take to define the scales of velocity and length, and henceforth set them to unity.

We first consider the flow with $W_0 = 2$. This is the largest ratio examined by

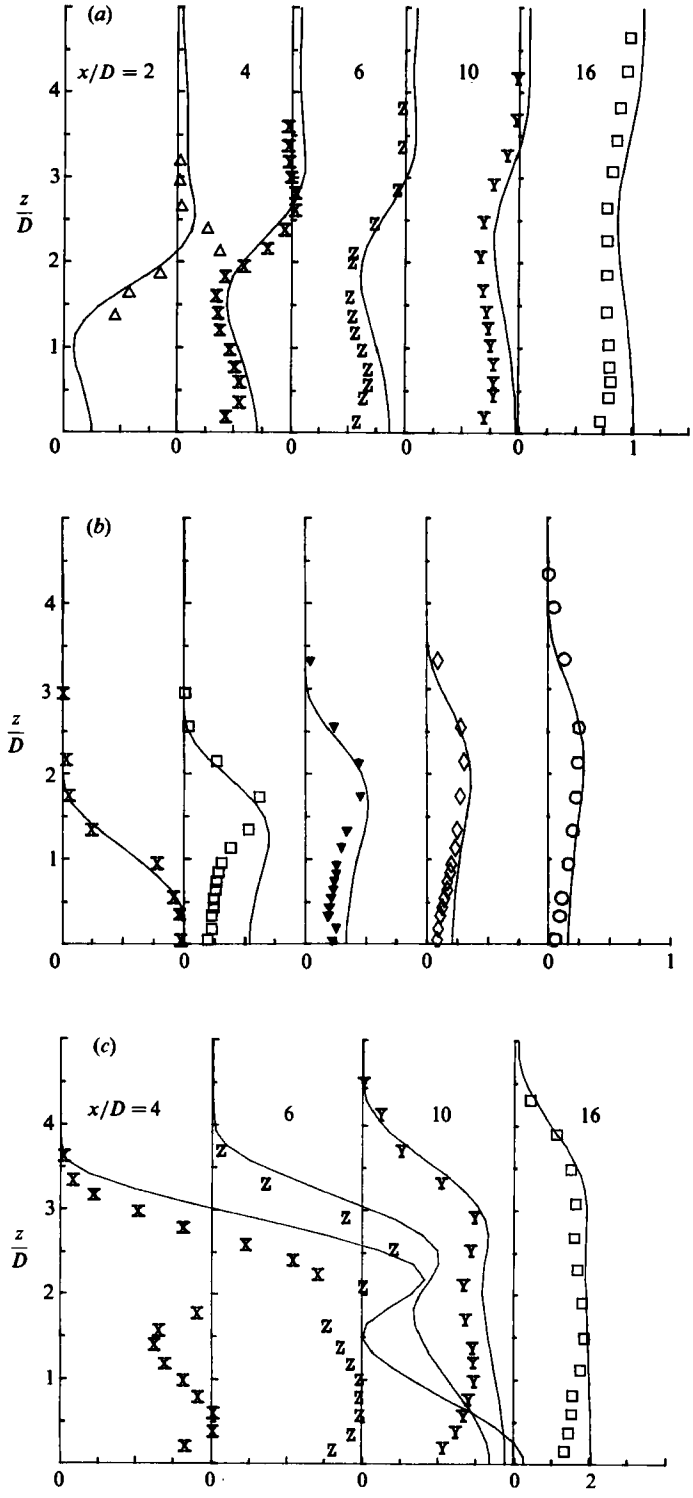

FIGURE 5. Comparison between predicted profiles at $y = 0$ for $R = 2$ and laboratory data. (*a*) Streamwise velocity component; (*b*) scalar field; (*c*) turbulence kinetic energy.

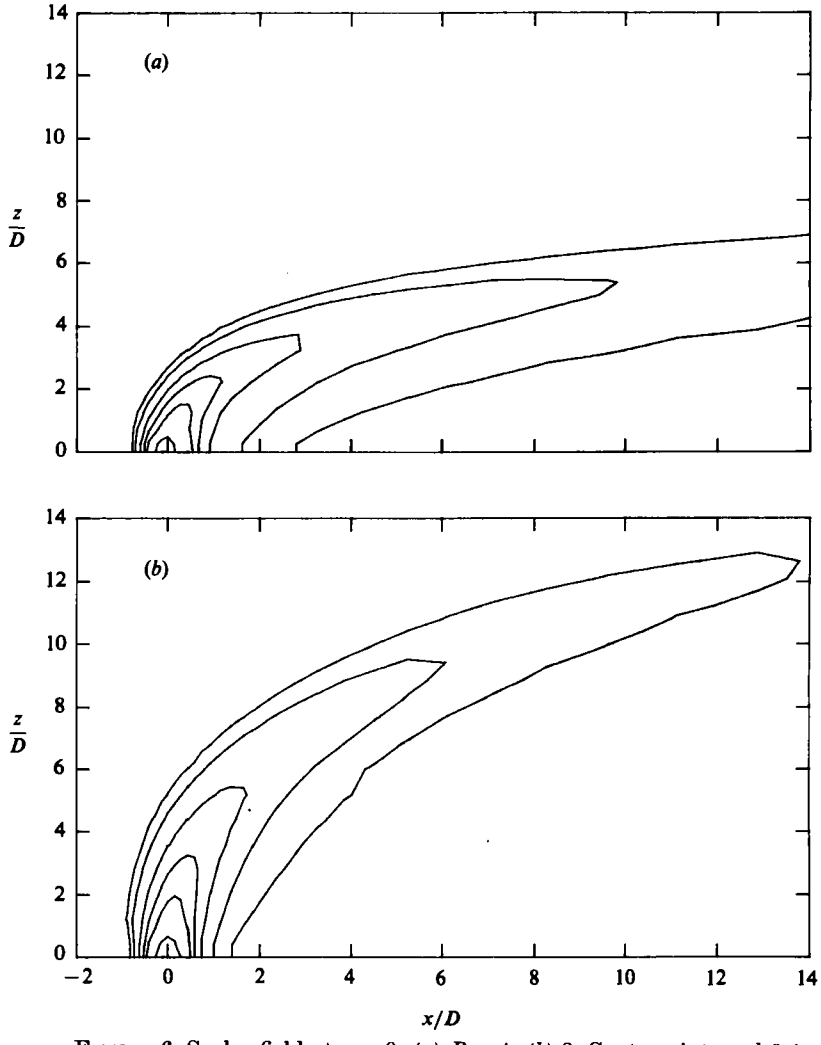

FIGURE 6. Scalar field at $y = 0$; (*a*) $R = 4$; (*b*) 8. Contour interval 0.1.

Andreopoulos & Rodi (1984), and there is evidence that the lower boundary does play a role but it is not dominant. Figure 1 shows a contour plot of the scalar field in the plane of symmetry. The trajectory of the maximum concentration shows a rapid rise to about $z = 2$ at $x = 2$, whereafter the jet rises very slowly, reaching $z = 2.5$ at $x = 10$. A similar plot in figure 2 for the x-component of velocity shows reversed flow immediately behind the jet; this is consistent with laboratory experiments which describe the initial jet as acting like a solid cylinder around which the free stream separates. There is some slight acceleration of the flow in the bending-over region, but the downstream flow is completely dominated by the wake effect of the slow-moving fluid entrained in the lee of the jet.

Transverse cross-sections of the scalar at $x = 6$ (figure 3) show a strong impact on the lower boundary, and relatively circular contours near the centre of the jet. The secondary-flow vectors at $x = 6$ are shown in figure 4, where the vortex pair system is clearly visible. The vortex centred at $x = 1$, $z = 1.5$ is slightly below and outside

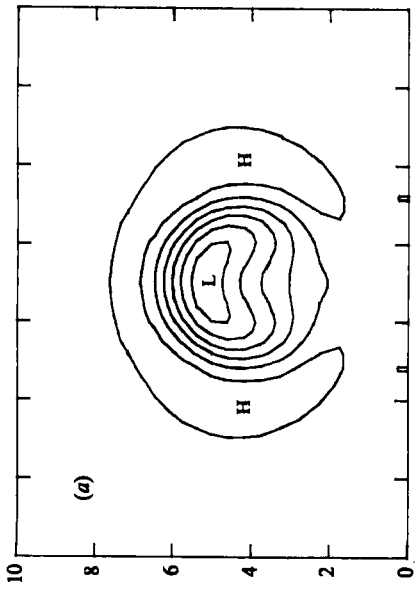

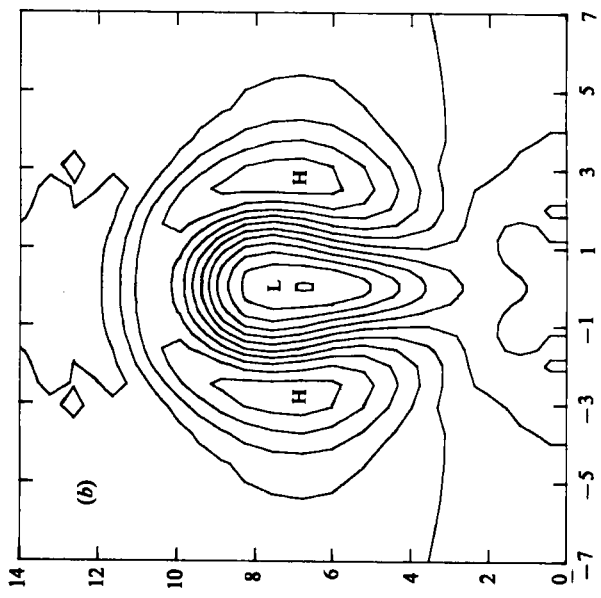

FIGURE 8. As figure 7, but for the streamwise velocity component. (*a*) Contour interval 0.05, max 1.05, min 0.8. (*b*) Contour interval 0.1, max 1.4, min 0.4.

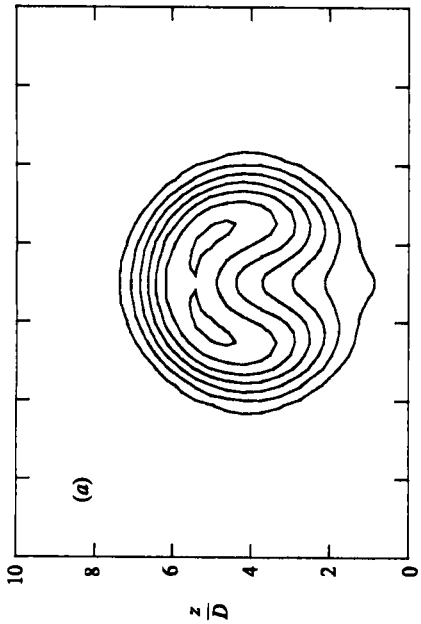

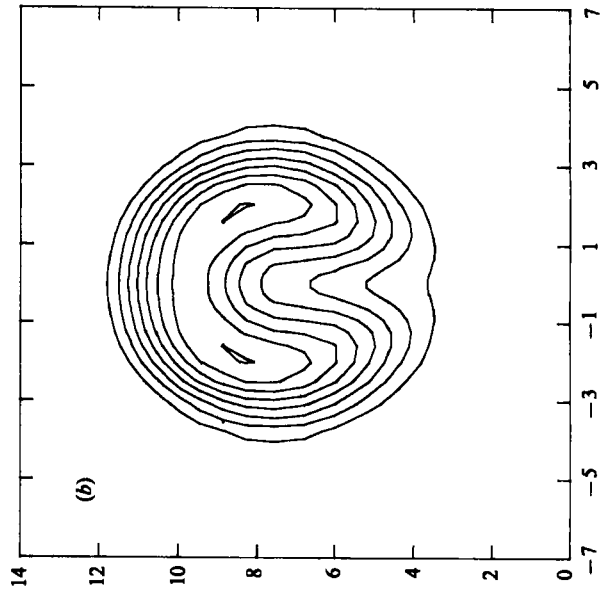

FIGURE 7. Transverse sections of scalar field; (*a*) $R = 4$, $x = 11.5$; (*b*) $R = 8$, $x = 6.5$. Contour interval 0.025.

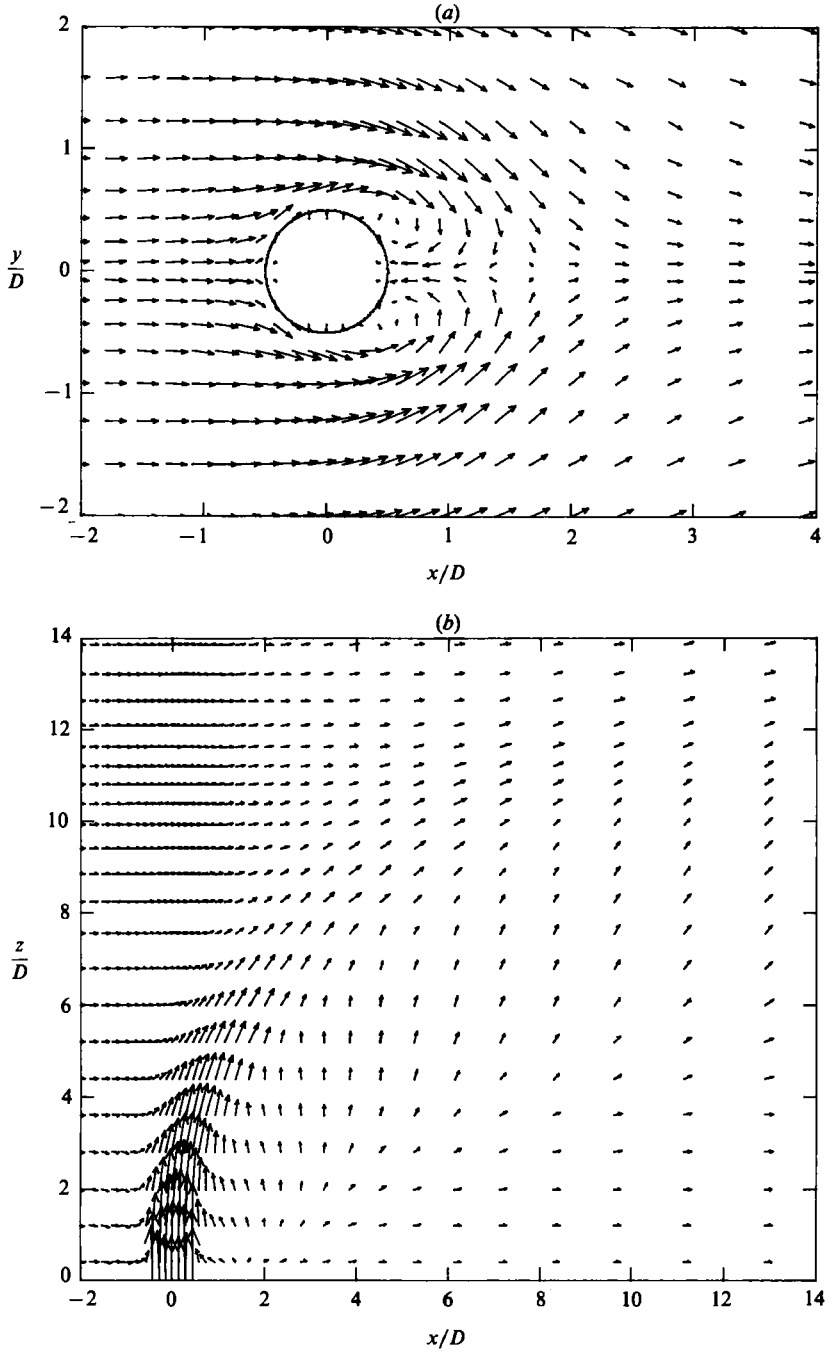

FIGURE 9. Flow vectors for $R = 8$: (*a*) horizontal plane, $z = 0$; (*b*) vertical plane, $y = 0$.

that identified in figure 6(*b*) of Andreopoulos & Rodi, but the velocity magnitudes are very similar.

Detailed cross-sections of streamwise velocity component, scalar concentration, and turbulence energy are compared with the experimental results in figures 5(*a–c*). The experimental data for the scalar field are from Andreopoulos (1983). The

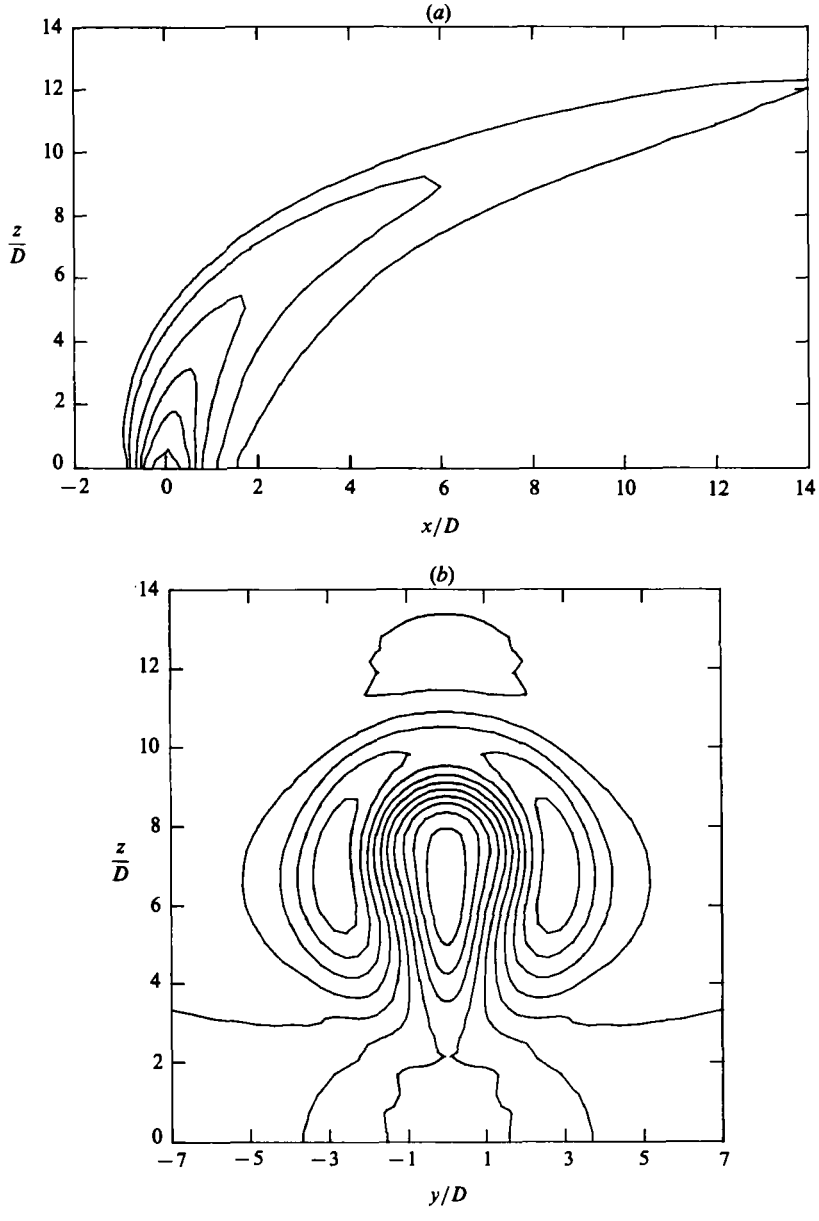

FIGURE 10. Contour fields for the high-resolution $R = 8$ integration: (*a*) Scalar field at $y = 0$; (*b*) Streamwise velocity component at $x = 6.5$. Contours correspond to figures 6(*b*) and 8(*b*).

agreement is not precise, but this must be due in part to the treatment of the lower boundary. The main discrepancy is in the value of q^2 near the lower boundary, which we overpredict. However, there is good agreement on the profile shapes and magnitudes away from the wall.

Figure 6 shows the scalar field in the plane of symmetry from the two runs with $W_0 = 4$ and 8. Comparison with the trajectories for the scalar maxima of Kamotani & Greber (1972) shows very good agreement. Transverse sections of the scalar field are shown in figure 7, and compare favourably with the laboratory measurements

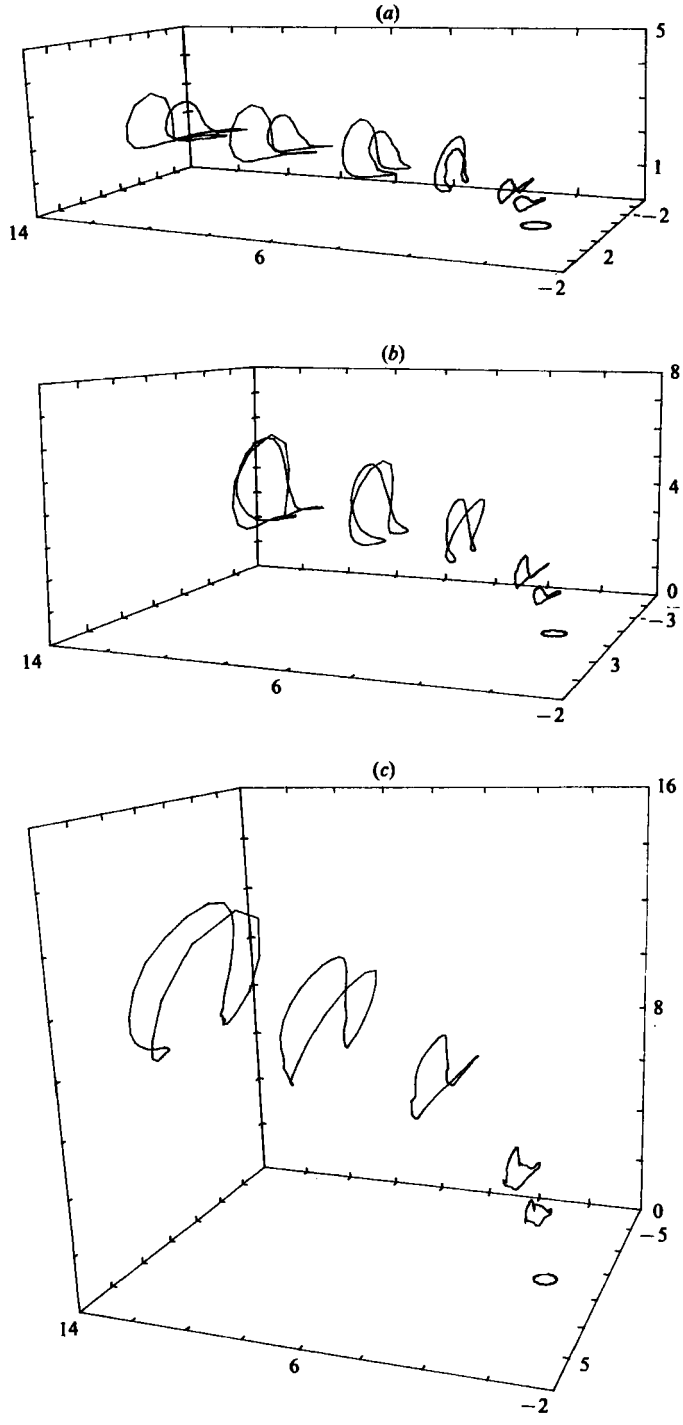

FIGURE 11. Perspective plots of the successive positions of a ring released at the jet exit: (*a*) $R = 2$; (*b*) 4; (*c*) 8.

in terms of the general size of the plume. The tendency toward splitting of the plume with higher exit velocity is apparent in figure 7, although the laboratory data show more difference between the two flows. Detailed comparison with the experiment is not warranted because the constant-density assumption utilized in the model is not appropriate for the early stages of the laboratory jet.

The x-component of velocity for the cases $R = 4$ and $R = 8$ are shown for transverse cross-section in figure 8. With $R = 4$, the velocity-defect region clearly dominates the downstream development of the jet, although there is a trace of higher-speed fluid above and to the sides. However, at $R = 8$ the transverse section at $x = 15$ shows significant regions of high-speed fluid which has been swept around into the vortices.

Some detail of the flow near the jet exit for the case $R = 8$ are illustrated by the velocity-vector plots in the horizontal and vertical planes ($z = 0$ and $y = 0$ respectively) shown in figure 9. The horizontal section shows a pattern typical of separated flow around a solid cylinder with acceleration around the sides and a reversed-flow region extending roughly 1.5 diameters downstream. However, the vertical section shows significant upward velocity in the lee of the jet, indicating convergence into the wake; this is the entrainment mechanism which brings environmental fluid into the jet.

One high-resolution integration was made to check numerical accuracy for these flows; the details are given in table 1 which shows an increase of roughly 75 % in the number of grid points in each direction for the case with $R = 8$. The scalar field in the plane of symmetry, and the transverse section of the streamwise velocity component are shown in figure 10: The contour plots are very similar to the low-resolution; apart from a slightly lower rise in the high-resolution case, differences are limited to a few percent at most. We can therefore have confidence in the numerical results as accurate solutions of the differential system described in the previous section.

As we mentioned previously, a major feature of a jet in a crossflow is the production of the vortex-pair system in the bending-over phase. The numerical solutions obtained above provide an opportunity for detailed examination of the flow, and in addition to the Eulerian cross-sectional plots, we have calculated particle trajectories through the flow to give some Lagrangian information. The simplest description of the initial jet is a vortex cylinder issuing vertically from the lower boundary, and in order to track the evolution of this vorticity, we have followed the trajectory of a ring of fluid particles which starts slightly above the boundary of the jet nozzle. Successive positions of the ring are shown in figure 11 for all three exit velocity ratios. All three flows show the same general distortion of the ring, viz. the sides of the ring are brought down below the middle part in the early stage of the bending-over phase. Only the $R = 8$ case shows a relatively undistorted ring more than one diameter from the nozzle.

In contrast to the particle trajectories, figure 12 shows vortex lines from the three flows which have been drawn by calculating trajectories in the three-dimensional vector vorticity field. The trajectories have been drawn in regions of significant vorticity, so that they illustrate the major vorticity features in the bent-over jet. There are many differences between the vortex lines, and the Lagrangian distortions of the ring in figure 11, and there are two reasons for the differences. First, the horizontal ring used as the initial condition for the particle trajectories is not a vortex ring; this is most clearly illustrated in the $R = 2$ vortex ring near the source, which shows the vertical component of vorticity in the sides of the ring due to lateral shear between the jet and the free-stream. The relative importance of the initial vertical component decreases with increasing R. The second factor causing the difference

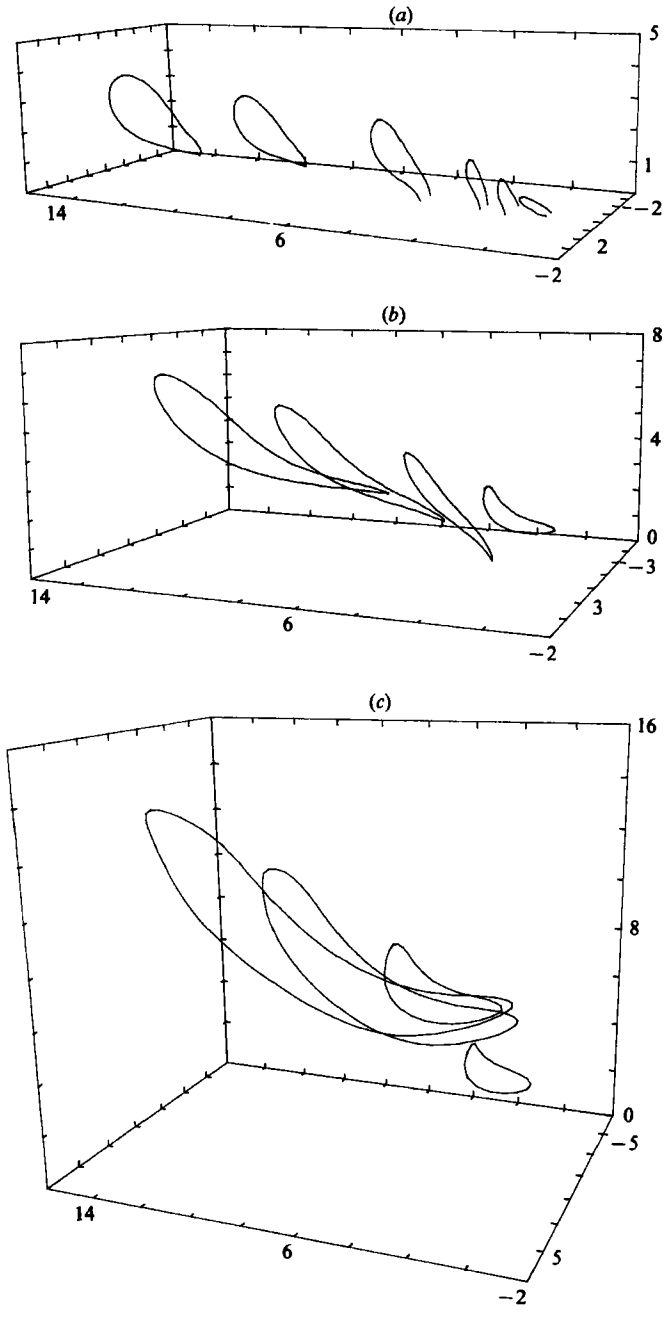

FIGURE 12. Perspective plots of vortex lines in the jet: (*a*) $R = 2$; (*b*) 4; (*c*) 8.

between the ring distortions and the vortex lines is diffusion, which is certainly important in these flows.

Using figures 11 and 12, we can gain insights into the dynamics of the jet flows. The highest velocity ratio, $R = 8$, is perhaps the simplest to understand, since this shows the greatest similarity between the vortex lines and the particle trajectories. The main difference is that the vortex lines are strongly stretched in the streamwise

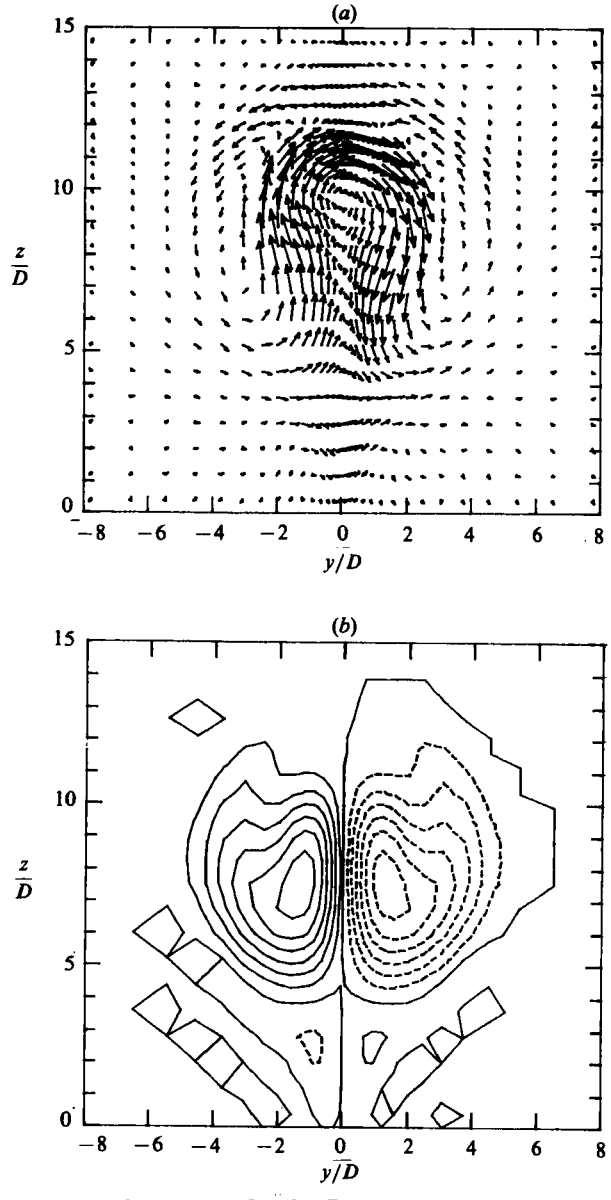

FIGURE 13. Vorticity field at $x = 10$ for the $R = 8$ jet: (*a*) transverse component, maximum vector of 0.40; (*b*) streamwise component, contour interval of 0.1.

direction. However, both fields show the loop bent down at the sides, and this can be seen more clearly in the transverse section of the vorticity field shown in figure 13. The transverse component is comparable in magnitude with the streamwise component, and has the same loop structure as the ring trajectory of figure 11. It seems likely that diffusion is responsible for the alignment of vortex lines in the stream direction, since the particle trajectories do not show evidence of stretching in that direction. Rather, diffusion reduces the transverse component in the ends of the loop more than the middle, which is undergoing lateral stretching as fluid is rotated outward and downward by the streamwise vortices. Furthermore, the lateral gradients of the streamwise velocity component are reduced by this diffusive effect,

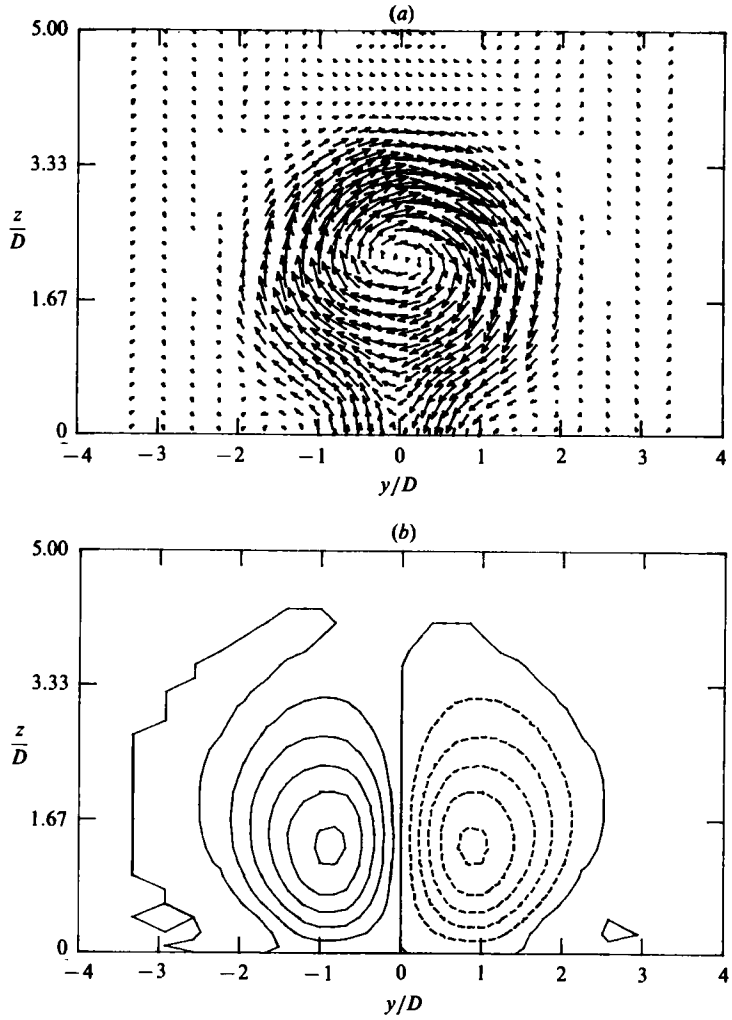

FIGURE 14. Vorticity field at $x = 10$ for the $R = 2$ jet: (*a*) transverse component, maximum vector of 0.26; (*b*) streamwise component, contour internal of 0.05.

which consequently reduces the streamwise separation of the particles while increasing the streamwise tendency of the vorticity vector. For this flow we therefore have a simple picture of vortex development as an initially horizontal ring which rises more rapidly in the centre and moves downstream, producing a simple loop containing streamwise vorticity in the sides. Thus, the vortex pair is really no more than the original streamwise vorticity in the sides of the jet, and the transverse component is diffused away in the ends of the loop, but is still significant in the central region.

The lower velocity ratios present a more complex picture, as the initial vertical vorticity component becomes more important. It seems likely that the surface boundary condition will play an important role in this case, but we presume that if the boundary layer was much thinner than the jet diameter on a non-slip lower surface, then the dynamics would not be changed. In the $R = 2$ case, we see that the initially tilted vortex ring has its vertical component strengthened rapidly to become an almost-vertical loop intersecting the lower boundary. We interpret the large vertical component as arising in the wake via the shedding of vertical vorticity as the flow 'separates' behind the jet, and the subsequent vertical stretching as the

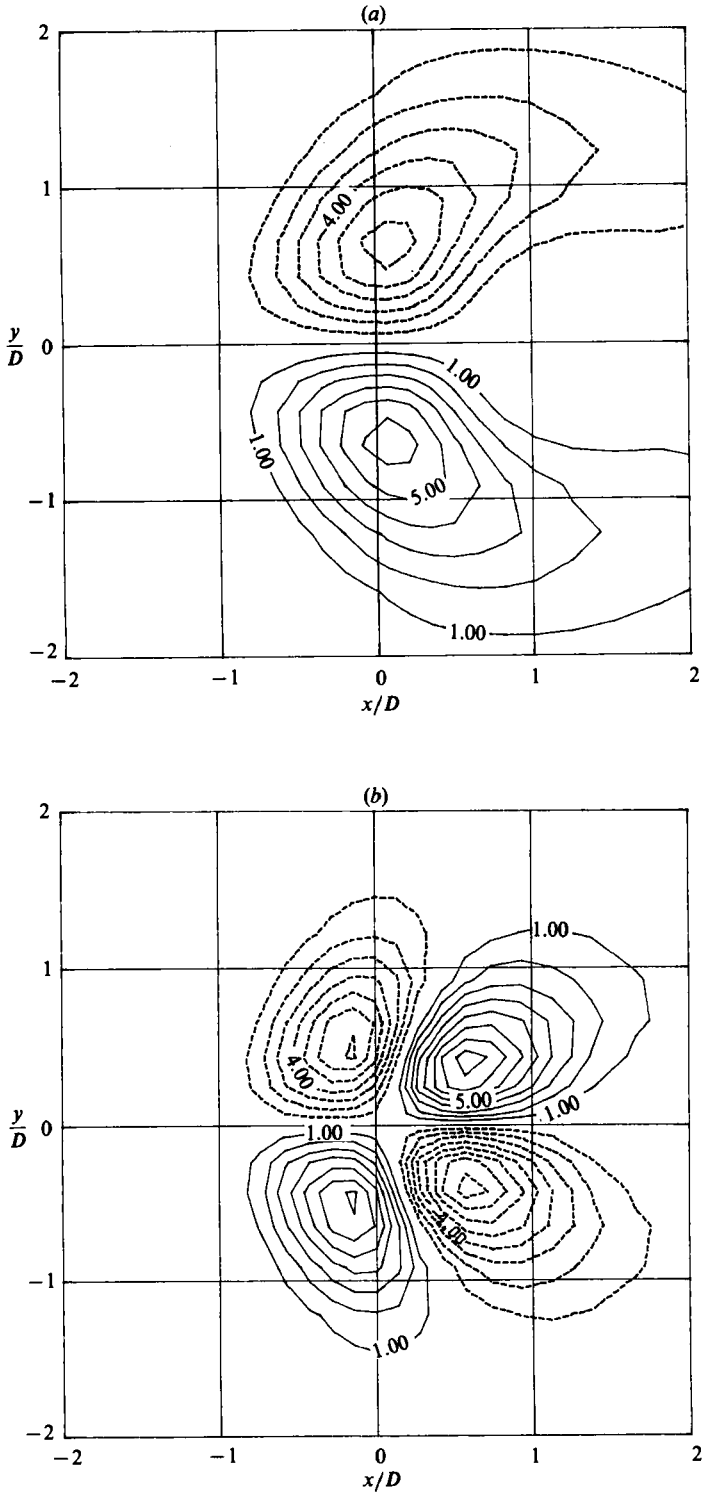

FIGURE 15. For caption see facing page.

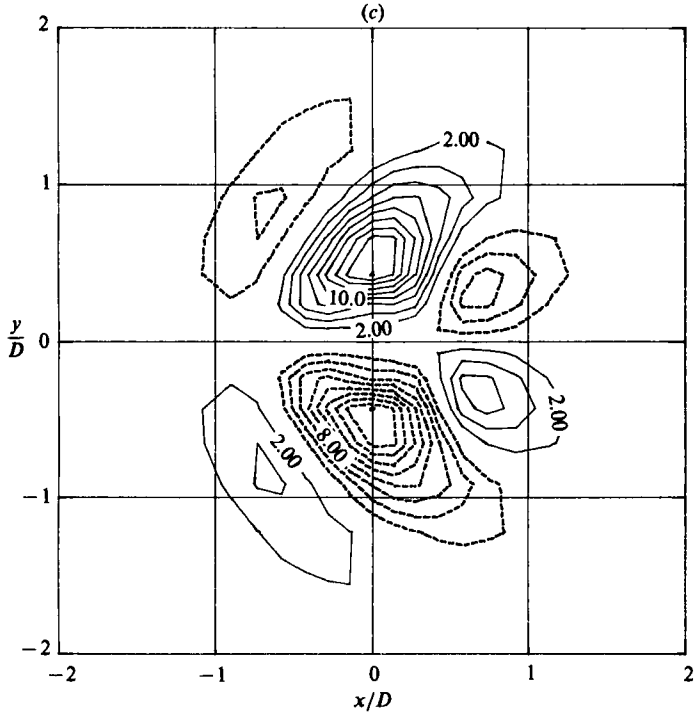

FIGURE 15. Horizontal cross-section at $Z = 2$ for the $R = 8$ jet. (*a*) Streamwise vorticity component ω_1; (*b*) vorticity production term P; (*c*) vorticity diffusion term, D.

wake is entrained upward with the jet. This vertical component remains in the transverse vorticity to dominate the loop structure shown in the particle trajectories. Thus, figure 14 shows that the transverse vorticity forms a simple ring which is not diffused as rapidly at the ends as in the $R = 8$ case. The streamwise component is still important for $R = 2$, but it no longer appears as a simple vortex pair. The relative weakness of the streamwise vorticity is presumably responsible for the dominance of diffusion in the scalar field for $R = 2$, which prevents the bifurcation of the plume.

We can provide further clarification of the vorticity dynamics by examining the details of the terms in the vorticity equation, i.e.

$$\frac{\mathrm{D}\boldsymbol{\omega}}{\mathrm{D}t} = (\boldsymbol{\omega}\cdot\nabla)\,\boldsymbol{U} + \boldsymbol{D}(\boldsymbol{\omega}),$$

where $\boldsymbol{\omega} = \nabla \times \boldsymbol{U}$ is the vorticity, and $\boldsymbol{D}(\boldsymbol{\omega})$ represents the diffusive term. We are interested mainly in the streamwise-component of vorticity, and therefore we shall look at $P = (\boldsymbol{\omega}\cdot\nabla)\,U_1$, and $D = D_1(\boldsymbol{\omega})$ at several locations in the jet.

Figure 15 shows ω_1 and the production and diffusion terms a short distance above the jet exit. The diffusion term is clearly dominant in the central portion of the vorticity distribution, and the production term is mainly a distorting effect. The production is mostly due to the acceleration of the background horizontal flows around the relatively stagnant jet; this produces vortex stretching on the upwind side and a corresponding enhancement of the vorticity, and the opposite effect downstream. However, the stretching terms are only about half the magnitude of the diffusion term at this stage.

As the jet bends through 45°, the dynamical balance is illustrated in figure 16. Here

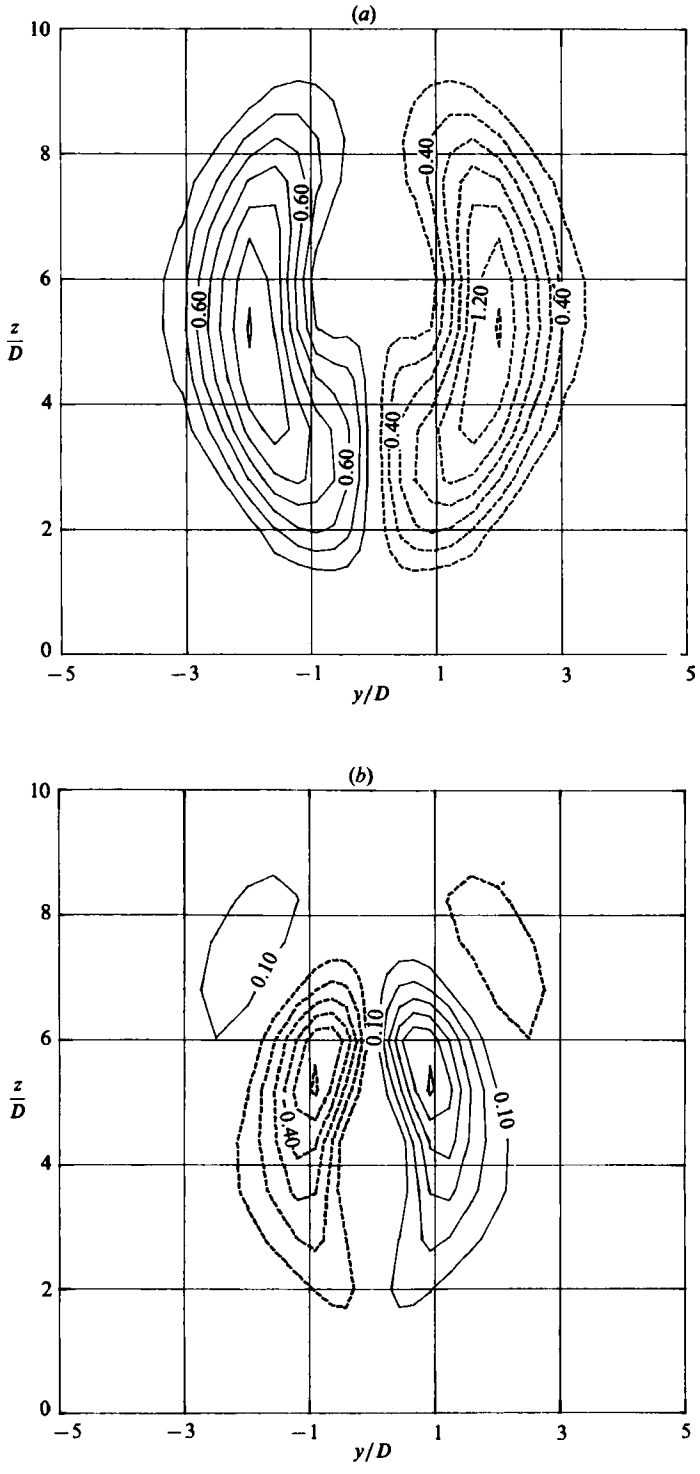

FIGURE 16. For caption see facing page.

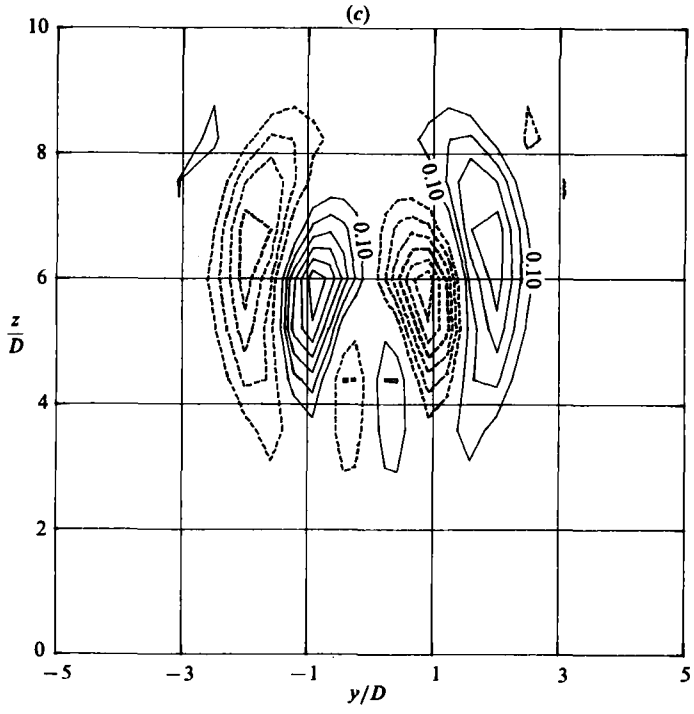

FIGURE 16. As figure 15, but a vertical section at $x = 3$.

the production term is consistently of opposite sign to the vorticity, and is therefore reducing its magnitude along with the diffusion term, which has a similar magnitude. The production term is centred inside and slightly above the centre of the vorticity distribution, and it prevents vorticity diffusion into the middle of the jet.

Further downstream at $x = 10$, figure 17 shows that diffusive effects are still dominant, while the production term is tending to strengthen the vortex near the central axis and reduce it further out. The mechanism for vorticity production here is the turning of cross-stream vorticity by the lateral velocity shear, but the effect is relatively weak.

From the preceding analysis of the vorticity dynamics, we conclude that the principal features of the flow are a result of injection of vorticity by the jet and subsequent diffusion of that vorticity. Inertial distortion of the vorticity field is not negligible, but it is small compared to diffusion, and does not produce any qualitative change in the streamwise vorticity. We have examined the highest-velocity-ratio case here and this flow showed the strongest inertial effects. Thus we expect the role of diffusion to dominate vorticity production throughout the range of velocity ratios considered.

4. Concluding remarks

The numerical solutions presented herein for the jet in a crossflow have provided insight into the dynamics of this three-dimensional flow. We have first compared our numerical results with laboratory data and obtained good qualitative agreement and reasonable quantitative agreement on most features. A further numerical check by

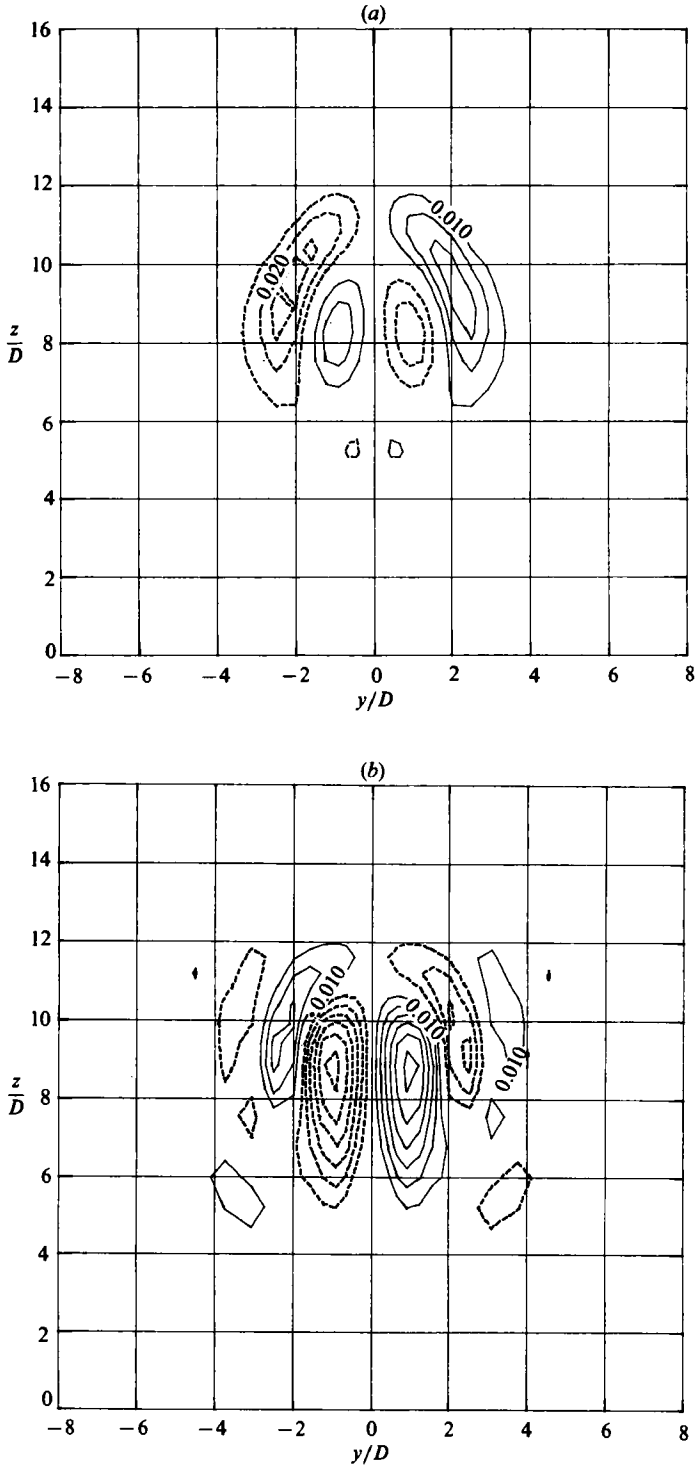

FIGURE 17. Vertical section at $x = 10$ for the $R = 8$ jet. Streamwise vorticity component is shown in figure 14(*b*). (*a*) Vorticity production term P; (*b*) vorticity diffusion term D.

means of a higher-resolution integration has given us confidence that we have a good numerical description of the flow field.

Examination of the flow has shown the development of the initial circular jet as it wraps around the slow-moving fluid which is entrained from the wake of the early part of the jet. For large exit-velocity ratios, this three-dimensional wrapping process distorts the initial rings of azimuthal vorticity into an apparent pair of horizontal line vortices by folding the sides downward under the action of the streamwise vorticity. The latter originates in the sides of the jet at the source, and dominates the sides of the jet where the transverse vorticity is diffused away. For lower velocity ratios ($R \leqslant 4$), the vertical component of vorticity at the source is important.

The dominance of diffusion over production in the vorticity equation suggests that the flow can be represented, at least qualitatively, by a series of vortex rings emitted from the jet source. The rings are advected and diffused, but as long as we can ignore the vorticity production terms they remain aligned in a horizontal plane. As the rings become diffused sufficiently for the free-stream advection to be larger than the induced velocity of the rings, the effects of the transverse components of vorticity in the rings are largely cancelled by the interaction between neighbouring rings. This gives the series of rings the appearance of a streamwise pair of line vortices.

This work was supported by the Electric Power Research Institute with G. R. Hilst as project manager.

REFERENCES

ANDREOPOLOUS, J. 1983 Heat transfer measurements in a heated, jet-pipe flow issuing into a cold cross-stream. *Phys. Fluids* **26**, 3201–3210.

ANDREOPOLOUS, J. & RODI, W. 1984 Experimental investigation of jets in a cross-flow. *J. Fluid Mech.* **138**, 93–127.

CHIEN, C. J. & SCHETZ, J. A. 1975 Numerical solution of the three-dimensional Navier–Stokes equations with application to channel flows and a buoyant jet in a cross-flow. *Trans. ASME* E: *J. Appl. Mech.* **42**, 575–579.

DEMUREN, A. O. 1983 Numerical calculations of steady three-dimensional turbulent jets in cross flow. *Comp. Meth. Appl. Mech. & Engng* **37**, 309–328.

FARNELL, L. 1980 Solution of Poisson equations on a nonuniform grid. *J. Comp. Phys.* **35**, 408–425.

KAMOTANI, Y. & GREBER, I. 1972 Experiments on a turbulent jet in a cross-flow. *AIAA J.* **10**, 1425–1429.

KEFFER, J. F. & BAINES, W. D. 1963 The round turbulent jet in a cross wind. *J. Fluid Mech.* **15**, 481–496.

LEWELLEN, W. S. 1977 Use of invariant modeling. In *Handbook of Turbulence* (ed. W. Frost & T. M. Moulder). Plenum.

MASON, P. J. & SYKES, R. I. 1979 Three-dimensional numerical integrations of the Navier–Stokes equations for flow over surface-mounted obstacles. *J. Fluid Mech.* **91**, 433–450.

MELLOR, G. L. & YAMADA, T. 1974 A hierarchy of turbulence closure models for planetary boundary layers. *J. Atmos. Sci.* **31**, 1791–1806.

MOUSSA, Z. M., TRISCHKA, J. W. & ESKINAZI, S. 1977 The near field in the mixing of a round jet with a cross-stream. *J. Fluid Mech.* **80**, 49–80.

ORLANSKI, I. 1976 A simple boundary condition for unbounded hyperbolic flows. *J. Comp. Phys.* **21**, 251–269.

PATANKAR, S. V., BASU, D. K. & ALPAY, S. A. 1977 Prediction of the three-dimensional velocity field of a deflected turbulent jet. *Trans. ASME* I: *J. Fluids Engng*, **99**, 758–762.

PIACSEK, S. A. & WILLIAMS, G. P. 1970 Conservation properties of convection difference schemes. *J. Comp. Phys.* **6**, 392–405.